



## Open Archive Toulouse Archive Ouverte (OATAO)

OATAO is an open access repository that collects the work of Toulouse researchers and makes it freely available over the web where possible.

This is an author-deposited version published in: <http://oatao.univ-toulouse.fr/>  
Eprints ID: 19929

To link to this article:

DOI:10.1016/j.msec.2018.05.029

URL:<http://dx.doi.org/10.1016/j.msec.2018.05.029>

**To cite this version:**

Stempflé, Philippe and Bourrat, Xavier and Pantale, Olivier and Njiwa, Richard Kouitat and Jehl, Jean-Philippe and Domatti, Anne and Lopez, Evelyne *Multiscale structure of nacre biomaterial: Thermomechanical behavior and wear processes.* ( In Press: 2018) Materials Science and Engineering C. ISSN 0928-4931

Any correspondence concerning this service should be sent to the repository administrator: [staff-oatao@listes-diff.inp-toulouse.fr](mailto:staff-oatao@listes-diff.inp-toulouse.fr)

# **Multiscale Structure of Nacre Biomaterial: Thermomechanical Behavior and Wear Processes**

Philippe Stempflié<sup>1\*</sup>, Xavier Bourrat<sup>2</sup>, Olivier Pantalé<sup>3</sup>, Richard Kouitat Njiwa<sup>4</sup>, Jean-Philippe Jehl<sup>4</sup>,  
Anne Domatti<sup>1</sup>, Evelyne Lopez<sup>5</sup>

<sup>1</sup>*Institut FEMTO-ST (UMR CNRS 6174, UFC, UBFC, ENSMM, UTBM), 15A Avenue des Montboucons, F-25030, Besançon Cedex, FRANCE*

<sup>2</sup>*BRGM LAB/MIN, 3 Avenue Claude Guillemin – 45060 Orléans cedex 1 – FRANCE*

<sup>3</sup>*Université de Toulouse, INP/ENIT, Laboratoire Génie de Production, 47 avenue d'Azereix, F-65016 Tarbes, FRANCE*

<sup>4</sup>*Institut Jean Lamour (UMR CNRS 7198 – INPL – Nancy University), Parc de Saurupt, F-54042 Nancy cedex, FRANCE*

<sup>5</sup>*Museum National d'Histoire Naturelle (UMR 5178 CNRS – MNHN), CP 51, 55 Rue Buffon, 75005 Paris, FRANCE*

## Abstract

Sheet nacre is a hybrid biocomposite with a multiscale structure, including nanograins of  $\text{CaCO}_3$  (97% wt.% – 40 nm in size) and two organic matrices: (i) the *interlamellar* mainly composed of  $\beta$ -chitin and proteins, and (ii) the *intracrystalline* composed by silk-fibroin-like proteins. This material is currently contemplated for the manufacture of small prostheses (*e.g.* rachis and dorsal vertebra prostheses) which are subjected to micro-slip or fretting motion. In this work, the tribological behaviour of nacre is studied by varying the frictional dissipated power from few nW to several hundreds mW, in order to assess the various responses of the different nacre's components, independently. Results reveal various dissipative mechanisms *vs.* dissipated frictional power: organic thin film lubrication, tablet's elastoplastic deformations, stick-slip phenomenon and/or multiscale wear processes, including various thermo-mechanical processes (*i.e.*, mineral phase transformation, organics melting and friction-induced nanoshocks process on a large range). All these mechanisms are controlled by the multiscale and anisotropy of its structure – and especially by its both matrices and respective orientation *vs.* the sliding direction.

**Keywords:** Nacre; Organic matrix; Multiscale analysis; Frictional dissipated power

\*Corresponding author: Stempflé Philippe (philippe.stempfle@ens2m.fr)

## 1. INTRODUCTION

Sheet nacre (the pearly internal layer of molluscan shells) is a biocomposite displaying an organomineral *multiscale* structure [1-6]. It exhibits high strength and toughness though it is primarily composed of a hard and very brittle ceramic – so-called aragonite (97%wt.) [7, 8]. The well-known nacre's superior mechanical properties lies in its hierarchical structure (Fig. 1) meaning that particular structures exist at distinct length scales. Thus, Dutta *et al* [9] first reported the importance of length scales in maximizing both load-transfer capability and resistance to crack initiation in composites both under static and impact rates of loading.

At the first hierarchical level (Fig. 1a), sheet nacre is usually described as a layered *brick & mortar* architecture [3, 7]: *bricks* corresponds to aragonite tablets (1-5  $\mu\text{m}$  long and 500 nm thick) while the *mortar* appears as an *interlamellar* organic matrix made of highly cross-linked protein of polysaccharide and b-chitin (30 nm thick) [2]. Although this organic matrix constitutes a few percent of the total weight of the shell (< 3%wt.) it has a significant influence on the overall mechanical properties of nacre, as demonstrated by many authors from years (eg. [2, 10-13]). Indeed, *interlamellar* layers of polymers act as energy absorbers which limit the propagation of cracks and finally avoid the formation of critical failure within the biocomposite [13].

However, recent works [4-6, 14] demonstrated a second hierarchical level which takes place within the tablet (Fig. 1b). The latter is indeed not purely mineral but is itself an organomineral composite – Fig. 1c and d – constituted by aragonite biocrystals (40 nm in size, Fig. 1e) drowned within a 4 nm thick *intracrystalline* organic matrix – constituted by silk-like proteins – organized as a tridimensional structure forming the micro-sized flat tablets (thickness about 500 nm, Fig. 1b) [15]. Hence, these tablets are further able to dissipate energy by elastic-plastic deformation leading to an overall increase in fracture toughness [14, 16].

Because its hierarchical structure is a great source of inspiration in the design of new kinds of composites, sheet nacre has been largely studied from decades by researchers and engineers [13, 17-20]. In particular, this material is currently being studied in two main research fields: (i) the creation of new organic /inorganic bio-inspired hybrid materials [13, 17-19] and (ii) the design of small prostheses [20-23]. In this framework,

classical approaches consist to strive to produce synthetic composites that display desired mechanical properties by mimicking the nacre structures at different scales [18]. On the one hand, investigations conducted by Dutta *et al.* [13] provided guidelines for designing light-weight and tough adhesively bonded structures and staggered architecture composites. On the other hand, Zhu *et al* [19] created a nacre-like material at the microscale which is composed of PMMA tablets layered as a columnar arrangement where interactions between layers are only controlled by the tribological aspects at the interfaces [24]. At a lower scale, Tang *et al* [20] created an interesting organic/inorganic nanolayered structure of polyelectrolytes and clays. Because this nanolayered material exhibits tensile strength and Young's modulus very close to the bone ones, it seems to be a good candidate for creating medical implants.

Another way followed by researchers is to looking at the possibility of using nacre for reconstructing human bodies [21-23]. Owing to its natural biocompatibility with human, nacre became an obvious candidate as a possible alternative to existing implant materials [8, 23]. Indeed, current implants display a lot of drawbacks which are mainly connected to tribological behavior such as unsatisfactory life time or wear particles-induced inflammatory reactions, for instance. Thus, Atlan *et al* [21] first tested nacre as a bone implant and showed that nacre implant triggers and encourages osteogenic – or bone forming – activity [22].

Taking into account the natural biocompatibility of nacre with bone as well as its tremendous durability connected to its great mechanical properties, this materials could definitely be considered as a potential substitute for defective bone [21-23] by direct implant or by creating some new organic/inorganic bio-inspired hybrid materials [20]. However, these challenging applications clearly need some knowledge about the frictional and wear behavior of this material [25-31].

Recent tribological results, obtained in dry friction [25-31] and in liquid medium [25], reveal that the wear mechanisms are strongly controlled: (i) by the environment itself, especially in liquid medium [25] through various physico-chemical interactions, occurring inside of the water-soluble *intracrystalline* organic phase [15]; and (ii) by the amount of energy dissipated during tribological tests in dry friction [e.g., 28]. Thus, as a function of the amount of frictional power dissipated within the multi-asperity tribocontact, nacre can be

submitted to peculiar thermal [27] and mechanical [25, 26, 30, 31] damage processes that occur at various orders of magnitude involving its double composite structure. This way, various *multiscale* wear mechanisms can be observed, leading to various wear rate levels, controlled by the *multiscale* structure of nacre *itself* [25-27, 29]. Besides, organic matrices are always directly involved in the friction-induced energy dissipation mechanisms and, in the subsequent damage mechanisms. So, the way the organic matrices control the wear mechanisms can be successively studied by varying the amount of frictional power, which is dissipated within the contact – that is, by changing the size of the *real contact area* (*i.e.*, the contact pressure) and the sliding velocity within a large range.

The aim of this work is to study each wear mechanism independently – as a function of its own frictional dissipated power – by using *multiscale* tribological tests. Thus, frictional dissipated powers range from few nanowatts (which is sufficient for inducing self-heating elastic deformation and/or long recovery-time viscoelastic deformation of the organomineral tablets [29]) to several hundreds milliwatts (which enable phase changes of the mineral phase [27, 28, 32, 33]).

## **2. EXPERIMENTAL PART**

### **2.1 Sheet nacre samples**

Samples are made of sheet nacre extracted from giant oyster *Pinctada maxima* [5, 29]. They are polished more or less parallel to the aragonite tablets orientation in a so-called *face-on* configuration (size: 5  $\mu\text{m}$ , thickness: 400 nm, Ra:  $14.5 \pm 0.6$  nm). Note that a residual angle (about  $8^\circ$  vs. the horizontal) is generally observed by AFM. The average size of the nanograins assessed by AFM image analysis is  $38 \pm 21$  nm (Fig. 1e). Mechanical properties of samples – and their components – are compiled in Table 1. Some of them have been measured by combining acoustic microscopy and spherical nanoindentation, as described in §2.2. The others were compiled from our previous works which used spherical and sharp nanoindentation tests coupled with homogenization theory [14, 26].

## 2.2 Mechanical properties of sheet nacre samples

Acoustic microscopy (AM) is a non-destructive method based on the use of ultrasonic waves [34, 35]. Mechanical properties of heterogeneous or multi-phased materials can be determined from the knowledge of the acoustic wave propagation velocity [36]. The acoustic waves are highly focused by an acoustic lens (482 MHz, see Fig. 2a) in order to obtain a good spatial resolution attaining a few micrometers. Two main operating modes are used [37] :

- (i) the *Imaging Mode* (Fig. 2) is a *qualitative* assessment which has a capacity for providing tomographic information related to stress fields associated to subsurface material discontinuities and damage. Using constant defocussing, *acoustic images* display qualitative information on the material structure or surface topography (Fig. 2b). When the lens is focused below the sample surface, buried structures appear, as shown in Fig. 2c for sheet nacre. This technique allows a clear distinction of tablets and interlamellar matrix from the different mechanical properties of the both mineral and organic phases.
- (ii) the *Acoustic Signature Mode* (Fig. 3) is a *quantitative* mode where elastic parameters such as Young's modulus and Poisson ratio local modulus can be measured with microprobe resolution. As shown in Fig. 3a, the so-called  $V(z)$  curve –  $V$  refers to the video or envelope-detected signal that is used to modulate the brightness of the picture, and  $z$  refers to the amount by which the specimen surface is displaced from the focal plane of the lens [34] – exhibits a strong pseudo periodicity that can be connected to specific surface acoustic wave velocity. Using signal processing based on a Fourier transform analysis (FFT, Fig. 3b) this period is accurately extracted to calculate the velocity of the surface wave responsible for these oscillations. For composite such as sheet nacre – which is composed of mineral and organic phases – two different signals can be obviously assessed. These

signals can be easily deconvoluted because the propagation velocity of acoustic waves is very different in the two phases.

From Acoustic Signature assessments, assuming linear elastic behaviour, the model links the standard elastic parameters such as the Young's modulus and the Poisson's ratio to the density and two specific velocities [36]:

$$E = \frac{3 - 4 \left(\frac{V_T}{V_L}\right)^2}{1 - \left(\frac{V_T}{V_L}\right)^2} \rho V_T^2 (Eq. 1) \quad \nu = \frac{2 \left(\frac{V_T}{V_L}\right)^2 - 1}{2 \left[\left(\frac{V_T}{V_L}\right)^2 - 1\right]} (Eq. 2)$$

where,  $V_L$  is the velocity of longitudinal waves, which create compression and traction stresses along the wave propagation direction; and  $V_T$  is the velocity of transverse waves whose induced shear strains are perpendicular to the wave propagation direction; and  $\rho$  is the density. However,  $V_T$  is not directly assessed in practice. Instead Rayleigh wave velocity,  $V_R$  is measured locally in addition to  $V_L$  from the FFT acoustic signatures (Fig.3). Equation 3 is used to get  $V_R$  from  $V_L$  and  $V_T$  in order to finally compute  $E$  and  $\nu$  using equations (1) and (2) :

$$V_R = V_T \frac{0.715 - \left(\frac{V_T}{V_L}\right)^2}{0.75 - \left(\frac{V_T}{V_L}\right)^2} (Eq. 3)$$

Various assessments need to be done at various defocusing distances. Defocusing is actually the process of decreasing the separation of the lens and specimen relative to the focal distance [34].  $V_T$  is finally computed using Eq. 3 formulated as :

$$V_T^3 - V_R V_T^2 - 0.715 V_L^2 V_T + 0.75 V_R V_L^2 = 0 (Eq. 4)$$



Only one root is physically acceptable in term of mechanical properties. However, it is worth of mentioning that Acoustic Microscopy fails to provide the whole elastic properties because the lack of equations *versus* the number of unknowns [37]. Indeed, one of the elastic properties – generally the Poisson’s ratio – needs to be known beforehand by means of another technique. Comte *et al* [37] demonstrated that nanoindentation can be combined with acoutic microscopy because the material volume which is involved during the test is in the same order. Thus, knowing the Poisson ratio evaluated by nanoindentation (Table 1), the Young’s modulus can accurately be deduced from  $V_R$  using the following relationships [36]:

$$E = k\rho V_R^2 (\text{Eq. 5}) \text{ with } k = \frac{2(1+\nu)^3}{(0.87+1.12\nu)^2} (\text{Eq. 6})$$

In practice, the systematic error was evaluated at 1.07% by using reference samples. Hence, the standard deviation of the Young’s modulus is evaluated at 5%. Three measurements have been done for each sample with five defocusing distances per point. As mentioned above, the resolution is evaluated at 3  $\mu\text{m}$  owing to the coupling liquid (distilled water). Experimental results give  $V_L = 2400$  Hz and  $V_R = 3250$  Hz leading to  $E_{\text{tablet}} = 58 \pm 5\%$  GPa and  $E_{\text{matrix}} = 13 \pm 5\%$  GPa, assuming the nacre density equal to 1.18 [2, 10].

For the organomineral tablets, Young’s modulus is in good agreement with the one previously measured using spherical nanoindentation [14] (see Table 1). This is not the case for the *interlamellar* matrix since its Young’s modulus is twice as that evaluated previously by spherical nanoindentation [26]. This difference is clearly connected to the presence of porosity within the *interlamellar* organic matrix. Indeed, spherical nanoindentation needs to use a structural model in order to extract the mechanical properties of each phase of a composite. The structural model used in our previous paper [26] is pictured in Fig. 4a. It considered the organic matrix as a continuous phase, in agreement with SEM analysis of Rousseau *et al* [5] which clearly demonstrated that interfaces between tablets of *Pinctada maxima*’s sheet nacre were only organic without

any mineral bridges. Using this structural model, the Young's modulus assessed at high loads spherical nanoindentation corresponds to the transversal Young's modulus ( $E_T$ ) of a stacking of layers made up of pure matrix and reinforced layers (mineral and organic). Its value is connected to the ones of the tablets  $E_f$  and the *interlamellar* matrix  $E_m$  by the following relationship which take into account the volume fraction of the tablets  $V_f$ , considering nacre as a composite of tablets and *interlamellar* organic matrix [26]:

$$E_T = \left( \frac{1}{E_f - E_m \left(1 - \frac{1}{\sqrt{V_f}}\right)} + \frac{1 - \sqrt{V_f}}{E_m} \right)^{-1} \quad (Eq. 7)$$

Using this relationship, spherical nanoindentation leads to a Young's modulus of the continuous matrix equal to 6.3 GPa as reported in Table 1 from [26] to be compared at 13 GPa obtained using acoustic microscopy.

As suggested in Fig. 2c, a new structural model of sheet nacre – which takes into account the matrix porosity – is needed to validate the AM's mechanical properties by using spherical nanoindentation. But how much porosity does the *interlamellar* matrix hold in? As shown in Fig. 5a, the void amount has been estimated *at minima* by discriminating the *interlamellar* matrix and its porosity in different transversal cuts observed in darkfield TEM. The minimum value of crossed porosity is about  $35\% \pm 5.6\%$ . Beside, other SEM preparations reveal a honeycomb structure in the *interlamellar* area under the tablets (Fig. 5b). Porosity is here estimated by stereology at  $59\% \pm 3\%$ . Thus, one can consider that our *Pinctada maxima* sheet nacre is constituted by an *interlamellar* matrix (6.47% wt.) which displays a porosity of about  $47\% \pm 25\%$ . We will see in §3 that this heterogeneity will strongly affect the wear mechanisms.

Knowing the amount of porosity within the *interlamellar* matrix, its mechanical properties can be now re-evaluated by using the previous spherical nanoindentation results applied but with a structural model which takes into account the porosity of the matrix (Fig. 4b). Thus, it appears that the previous matrix Young's modulus (*ie* 6.3 GPa) is no longer that of a continuous matrix but the one of the composite layer which is

constituted by organic matrix and voids. Assuming the Young's modulus of the pores equal to zero and the above ratio of porosity, the *real* Young's modulus of the *interlamellar* matrix is now re-evaluated at 13.5 GPa, which is in good agreement with both the value assessed by acoustic microscopy, and the one reported by Xu *et al* – ie.,  $11 \pm 3$  GPa [38].

### **2.3 Thermal properties of sheet nacre – Scanning Thermal Microscopy**

The local thermal properties of the samples, and especially the relationship between the frictional dissipated power and the contact temperature are assessed with a SThM (*TA Instruments  $\mu$ TA 2990* with a *TA Instruments controller TA 5300*, New Castle, DE), which is an analytical system that combines the high resolution visualization and positioning methods of scanning probe microscopy with the technology of thermal analysis [27]. The standard AFM probe is replaced by a thermal probe made from a Wollaston wire (5  $\mu$ m diameter platinum – 10% rhodium wire enclosed in a silver sheath), which allows the acquisition of the surface contact temperature, and simultaneously acts as a highly localized heater. The vertical deflection of the assembly is monitored by a light pointing technique. Spring constant is  $10 \text{ N.m}^{-1}$ . The constant current setpoint and the z-setpoint are 1 mA and 50 V, respectively. The scanning rate of the probe is  $100 \mu\text{m.s}^{-1}$ . The latter is sufficiently weak so that the heat transfer regime stays in the steady state conduction as in the high power tribological tests. The spatial resolution and the thermal sensitivity are about 100 nm and  $1^\circ\text{C}$ , respectively. Calibration of the SThM and procedure are detailed in [28].

### **2.4 Multi-scale tribological tests**

#### *2.4.1 Macro-tribological tests (1 - 630 mW)*

The experimental device is a *pin-on-disc* tribotester CSM Instruments (Peseux Switzerland) [28]. High power tribological tests are carried out at ambient air and room temperature in dry conditions by repeated friction of a 3.5 mm square shaped pin of nacre against the surface of a polished disc of nacre ( $\varnothing$  44 mm). The total sliding distance is about 100 m. Frictional dissipated power varies within the range of 1 to 630 mW by changing the normal load from 1 to 15 N (with a sliding velocity fixed at  $v = 10$  mm/s) or the sliding velocity from 1 to 150 mm/s<sup>-1</sup> (with a normal load fixed at  $F_n = 10$  N), respectively. According to the mechanical and thermal properties of samples, the situation during the macrotribological tests closely approximates the steady state thermal conduction [28, 39].

Wear rates are determined at the end of tests by measuring the weight of the material lost during the tests (precision: 10<sup>-4</sup>g). Any phase transformation of the wear debris is assessed using X-Ray diffraction. However, wear debris generated in dry friction are generally constituted by agglomeration of elemental nanodebris [25]. In order to assess the real size of the elemental wear debris – leading to the actual wear mechanisms occurring at the nanoscale – before any agglomeration process, wear particle size distribution measurements were conducted by using Photon Cross-correlation Spectroscopy (PCCS, NanoPhox, Sympatec, Germany [40]) in addition to traditional SEM and AFM observations. This technique extends the well-established principle of Photon Correlation Spectroscopy [41] to highly dilute suspensions. Prior any analysis wear debris are dispersed in distilled water with an ultrasonic bath. Then, the technique involves passing a laser beam into the suspension and measuring the Doppler shift of the frequency of dynamic light scatter at an angle with respect to the incident beam. This shift is related to particle velocity, which in turn, is inversely related to the particles size. Photon Cross-correlation Spectroscopy (PCCS) allows the measurement of elemental wear debris in the size ranges of about 1 nm to some  $\mu\text{m}$  [40].

#### 2.4.2 Multi-asperity nanotribological tests (2 nW – 0.1 mW)

The experimental device is constituted by a *ball-on-disc* nanotribometer CSM Instruments (*Switzerland*) [29]. A pin is mounted on a stiff lever, designed as a frictionless force transducer ( $K_x = 265.1$  N.m<sup>-1</sup> ;  $K_z = 152.2$  N.m<sup>-1</sup>). The friction force is determined during the test by measuring the deflection of the elastic arm

(low load range down to 50  $\mu\text{N}$ ). The ball ( $\text{Si}_3\text{N}_4$  –  $\approx 1.5$  mm) is loaded onto a flat nacre sample with a precisely known force using closed loop. The load and friction resolutions are about 1  $\mu\text{N}$  [42]. Tribological tests are carried out in linear reciprocating mode at room temperature (22°C) under ambient air (RH 35%). The sliding distance is about 10 m. The frictional dissipated power varies in the range of 2 nW to 0.1 mW by changing the normal load from 10 to 80 mN (at  $v = 1$  mm/s) and the sliding velocity from  $10^{-3}$  to 28 mm/s (at 40 mN), respectively. The thermal contribution is here greatly limited and clearly too low for damaging the matrices [29, 39].

At this scale classical *post mortem* wear analysis – like profilometry or AFM assessment – is not really suitable because (i) the error in wear assessment owing to the elastic recovery is no longer negligible and (ii) the presence of nanometric tribolayer within the contact cannot be taken into account when the contact is opened afterward [43]. In other words, *post mortem* assessment can only be used when the wear level is much more significant than the deformation one. Hence, an *in situ* wear assessment is carried out by using a real-time depth measuring sensor on the nanotribo-meter [42]. The depth range varies from 20 nm to 100  $\mu\text{m}$  with a resolution of about 20 nm. Tribological assessments are compiled using a *triboscopic* approach giving simultaneously, and for each cycle: (i) the *power map* (e.g., Fig. 17a) plotting the evolution of the power dissipated by friction along the friction track (this power is the product of the friction force by the sliding velocity ie,  $P_f = F_f \cdot v$ ) ; (ii) the *wear map* (e.g., Fig. 17b) which reveals any-time dependent wear process and/or potential build-up of a tribolayer within the contact. This map is computed from an *in situ* depth map by taking into account the tilting and the initial deformation of the samples, as reported previously [43]. Finally, an *in situ* wear rate assessment can be directly extracted from this *wear map* as a classical profile analysis (e.g., Fig. 17c) by using a topographical software (<http://gwyddion.net/>). The complete *in situ* wear assessment procedure has been described previously [43].

#### 2.4.3 Numerical simulations of wear process

In addition to experimental multiscale tribological tests, Finite Element (FE) simulations are carried out in order to understand elemental wear mechanisms that occur during the tribological tests, especially in the

range which is not investigated experimentally (in between 0.1 to 1 mW). As shown in Fig. 6, FE model simulates the effect of a rigid impactor on nacre sample *with* and *without* any shock occurrence. The associated damage mechanism will be analyzed and correlated to the results of tribological tests – as the assessment of wear debris, for instance. Numerical simulations need the mechanical properties – assessed using acoustic microscopy and nanoindentation – reported in Table 1. Besides, the numerical model will be able to simulate the influence of the matrix's porosity by keeping the matrix continuous while its Young's modulus will be changed from 6.3 to 12.6 GPa.

In practice, *Abaqus Explicit FEM* code [44] is used to solve the problem. The choice of an explicit code is connected to the presence of severe non-linearities induced both by the large deformations and the behavior laws that are used [44]. The mesh of each component has already been described in details [26]. We just point out that a ductile damage law is coupled with the erosion algorithm of the *Abaqus Explicit* code [44] to simulate the wear process. Thus, when the ductile damage criterion is reached, the corresponding element is considered instantly completely damaged, and is removed from the FE model. The ductile damage law is based on the maximal equivalent plastic strain value ( $\epsilon_{\max}$ ) of the *interlamellar* organic phase (10%), which is extracted from the work of Ji and Gao [45]. The plastic deformation of the organomineral tablets is assumed to be controlled by the *intracrystalline* organic matrix surrounding the nanometric biocrystals [14]. Therefore, the maximum strain value of the tablets is estimated from the volume fraction of the organic matrix, within the tablet, assessed by AFM image analysis – about 12% in 2D corresponding to 4.2% in 3D [14]. Thus, the maximum strain value  $\epsilon_{\max}$  of tablets can be estimated to be about 12% of the one of the interlamellar organic matrix ( $\epsilon_{\max} = 10\%$ , see Table1) because both presented models are bi-dimensional ones.

### 3. RESULTS AND DISCUSSION

#### 3.1 Evolution of the tribological behavior for the high power tribological tests ( $P_f > 1$ mW)

Figure 7 shows the variations of the dissipated power by friction –  $P_f = \mu F_n v$  – as a function of the sliding distance for various normal loads (2 N to 15 N). After a running-in period, the deduced friction coefficient is about  $0.44 \pm 0.02$ . This value also appears quite insensitive to any variation of the sliding speed in the range 1 to 150 mm/s. Thus, surprisingly the friction coefficient stays constant when the frictional dissipated power varies from 1 to 630 mW.

In contrast, wear rate is very sensitive to the frictional dissipated power, as reported in Fig. 8, which displays the effect of any change of normal load (Fig. 8a) and sliding velocity (Fig. 8b), respectively. Thus, various abrupt changes are observed when the frictional dissipated power exceeds 22 mW, 53 mW and 213 mW, respectively, whereas in the same time, the friction coefficient does not change and stays constant at  $0.44 \pm 0.02$ . This peculiar behavior is probably due to the presence of a tribolayer covering the friction track, which controls the frictional behavior as a negative feedback loop [46]. However, the various rises of the wear rate can be studied independently, by considering the various thermomechanical effects that are likely to occur within the contact.

### 3.1.1 Thermal – induced wear process at the highest frictional powers

Wear debris generated under various levels of frictional dissipated powers are assessed using X-Ray diffraction, and compared to the original spectrum of aragonite in Fig. 9. The intensity of the *calcite* peak (expected at  $34.28^\circ$  in Fig. 9) – *i.e* the other crystallographic form of the  $\text{CaCO}_3$  – gradually increases when the frictional dissipated power increases from 10 to 103 mW. Below 22 mW, the proportion of calcite in the wear debris is similar as the one that is assessed in the *Pinctada maxima* original spectrum. It is worth of noting that the irreversible transformation of calcium carbonate from *aragonite* to *calcite* only occurs when the temperature reaches  $470^\circ\text{C}$  [32, 33]. Thus, these results show that high temperatures can be briefly reached, at the level of the microscopic asperities, when the frictional dissipated powers exceed 50 mW (Fig. 9), leading to a phase transformation of the mineral part of the wear debris. Besides, cathodoluminescence assessments carried out on the tribolayer covering the friction track, reveal that this latter is also completely transformed to calcite [28].

However, since thermal-induced structural changes of the mineral are observed when the frictional dissipated power is higher than 22 mW, the temperature that drives the melting of the organic phases should be reached for the lower dissipated powers – somewhere in-between 1 and 20 mW. An accurate value of this latter can be assessed using a Scanning Thermal Microscopy [28, 39]. Practically,  $\mu$ DTA curve (Fig. 10a) reveals the relationship between the dissipated power and the contact temperature, and  $\mu$ TMA curve (Fig. 10b) simultaneously displays the change of the vertical displacement of the cantilever, as a function of the contact temperature. Whereas the continuous rise of the sensor *vs.* the contact temperature corresponds to the thermal expansion of the nacre sample (Fig. 10b), sensor jumps which are observed beyond 225°C clearly reveal that the tablets get unstuck when the organic phase is degraded in the slot of temperature 200°C to 350°C [24, 28]. Besides, the amplitude of the sensor's jumps of 250 to 500 nm appears very close to the value of the tablet's thickness. AFM views (Fig. 10b, inset), carried out before and after heating, confirm the matrix degradation as soon as the contact temperature exceeds 225°C. Finally,  $\mu$ DTA plot (Fig. 10a) provides an accurate value of the minimum thermal power that is necessary for melting the organic phase (about 17 mW).

Thus, these various X-Ray and SThM observations enable us to explain the tribological results (Fig. 7) and the variations of the wear rate *vs.* the frictional dissipated power (Fig. 8), by comparing the thermal response of sheet nacre (Fig 10a) with the thermal power which is really dissipated by friction during the tribological tests (Fig. 7). Assuming this latter being around 98% of the frictional power, macrotribological results reveal that:

- The first abrupt change of the wear rate (around 22 mW in Fig. 8) can be attributed to the degradation of the surface organic matrices ( $T_c \square 282^\circ\text{C}$  at 24.5 mW in Fig. 10a), when the frictional dissipated powers are greater than 17 mW. Indeed, this friction-induced contact temperature rises up to the melting point of the organic matrices, as observed in Fig. 10b.
- The *aragonite-calcite* phase transformation (expected around 470°C [32]) is clearly observed within the contact when the frictional dissipated power is higher than 49 mW. This value is extrapolated from the SThM curves at  $T_c \square 508^\circ\text{C}$  and is in good agreement with the calcite peak observed in Fig. 9 [33]. So,



this phase transformation well corresponds to the second change of the slope of the wear rate, that is observed in Fig 8b around 53 mW.

- Finally, the *avalanche effect* observed beyond 213 mW (Fig. 8b) could be attributed to the propagation of the heat flow within the subsurface when the steady state regime is reached. So, the matrix can be degraded in depth, leading to an increased rate of the wear.

Thus, for this range of dissipated powers ( $P_f > 17$  mW), wear of sheet nacre is clearly induced and controlled by thermal effects – combining melting of the organic matrices and friction-induced phase transformation of the mineral phase. Besides, for lower power levels ( $P_f < 17$  mW), the frictional-induced thermal component is not sufficient for melting the organic matrices ( $T_c < 210^\circ\text{C}$ ). Thus, another kind of wear mechanism must occur in this range of frictional dissipated powers as documented in the following.

### 3.1.2 Shock-induced wear process, at medium frictional powers

Typical AFM views of the friction track (Fig. 11a) can be seen after tribological tests conducted in the range of 1 to 17 mW. Nacre tablets are clearly crumbled; the edge lines are rough and let appear the nanograins constituting biocrystals. As a result, wear debris are very heterogeneous in size because they are constituted by single biocrystals, agglomerates, pieces of tablets and tablets as observed by PCCS (Fig. 11b). Obviously, this wear mechanism involves both organic matrices, *ie. intracrystalline* and *interlamellar*.

In order to explain how these matrices work together in this peculiar wear mechanism, numerical simulation using FEM models is carried out by varying the sliding velocity of the slider (so-called *impactor*) in the range of 10 down to 1 mm/s. These velocities enable us to extrapolate results to the lowest dissipated powers in order to make the connection with the next nanotribological tests. As mentioned above, a ductile damage law is coupled with the erosion algorithm of the *Abaqus Explicit* code to simulate the fracture inside both materials [44]. Thus, when the ductile damage criterion is reached, the corresponding element is considered instantly completely damaged, and is removed from the FE model. The intercrystalline matrix is first considered as continuous without any porosity.

Figure 12 shows simulation for two impactor velocities – *i.e.*, two dissipated powers – as observed at the same time increment ( $4 \cdot 10^{-2}$ s). Although both matrices are clearly solicited, major part of the fracture is located inside of the aragonite tablet whatever the impactor velocity (Fig. 12). This is the main consequence of the dynamic effects, and the presence of repeated shocks. Figure 13 illustrates the shock-induced wear mechanisms leading to the formation of elemental wear debris, the size of which is very close to the initial biocrystals one, as observed from a typical tribolayer AFM view (Fig. 13). Besides, stress distribution shows that during the impact, the ratio between the equivalent stress and the yield stress ( $\sigma/\sigma_y$ ), inside of the biological *interlamellar* organic matrix, is lower than the one inside of the tablet. The fracture propagation inside the *interlamellar* organic matrix is clearly limited: tablet's debonding does not occur. Hence, fracture inside the tablet leads to the formation of pieces instead of whole tablet.

However these numerical results seems to disagree with the experimental PCCS assessments (Fig. 11) which reveals a multimodale distribution rather as a monomodale one, as it could be suggested by simulations. Henceforth, new numerical simulations have been carried out by introducing the presence of porosity within the interlamellar matrix. This porosity is taken into account by keeping the matrix continuous while its Young's modulus is increased from 6.3 to 12.6 GPa. As shown in Fig 14a, crack propagation progressively moves outside the tablet when porosity ratio increases to finally occur inside the organic matrix leading to the formation of larger wear debris. Thus, the multimodale distribution of wear debris, see in Fig. 11B, can be satisfactorily understood by keeping in mind the large standard deviation that has been determined for the *interlamellar* matrix porosity – *ie.*  $47 \pm 25\%$ .

As a result, the complete damage mechanism involves here the fracture of both matrices, explaining the experimental high friction coefficient generally observed in this range of frictional powers ( $\mu = 0.44 \pm 0.02$ ) [9]. In addition, these simulations enable us to satisfactorily explain the formation of nanometric wear debris – as observed in Fig. 11 and 13 – which have a size very close to that of the initial nanograins constituting the tablets (Fig. 1e vs. Fig 13). In addition, simulations reveal that nanodebris can be directly generated

without subsequent tablet's crushing (Fig. 13). This mechanism is mainly due to the high velocity-induced shocks which occur within the tablets. This fracture behavior is also observed when the impactor's velocity is decreased by a factor 10 (*i.e.*, 1 mm/s, Fig. 12b), so this friction-induced nanoshocks mechanism is likely to be the driving force that controls the wear mechanism of nacre on a large range. Is this mechanism still licit at the lower power tribological tests as observed in multi-asperity nanotribological tests?

### **3.2 Evolution of the tribological behaviour for the low power tribological tests ( $1 \text{ nW} < P_f < 0.1 \text{ mW}$ )**

In the range of low dissipated powers, there are two different tribological regimes (Fig. 15a); this is in contrast to what is observed in the previous high power tribological tests, where only one single high level frictional regime is observed ( $\mu = 0.44$ ), controlled by a tribolayer of heterogeneous wear debris. First, a *high frictional regime* is very close to the one observed in our macrotribological experiments (§3.1). Second, a *low frictional regime* is only observed on a very smooth surface. The transition to the upper regime clearly occurs when the slider crosses cracks with a critical depth higher than the thickness of a tablet (more than 500 nm), as shown in Fig. 15b. So, any significant change in the roughness can involve this transition from low to high frictional regime. Which component is likely to control this transition?

#### *3.2.1 Nanotribological tests involving the high frictional regime*

As shown in Fig. 15a, the *high frictional regime* displays a high level coefficient of friction ( $0.35 \pm 0.15$ ), which is very unstable and close to the one observed in the high power macrotribological experiments ( $0.44 \pm 0.02$ ). Obviously, these high friction values are connected to a high wear rate, which is assessed using a phase-shifting interferometric profilometer (20 nm/cycle/N). Despite of the high frictional regime, there is no thermal-induced phase transformation here as revealed by the Raman spectrum carried out within the friction track after sliding (Fig 16). Since classical *post mortem* analysis is here useless, an *in situ* analysis should help to go further.

Figure 17 displays the typical *in situ* tribological behavior as observed in the *high frictional regime*. The average frictional power dissipated during this test is around 21  $\mu\text{W}$ . As shown in the Fig. 17a, the *power map* is very unstable along the friction track and also in time. This is because a heterogeneous tribolayer is continuously built-up and removed within the contact, as reported in the *wear map* (Fig. 17b). In order to estimate the amount of wear debris trapped within the contact, the tribolayer's thickness is computed from a *profile analysis* (Fig. 17c), carried out on the respective *wear map* (Fig. 17b). Its thickness evolves with the number of cycles but, it increases and even overshoots several micrometers. Thus, this thickness is always higher than a *single* tablet's thickness (about 500 nm), revealing that *several layers* of tablets are probably involved in the wear process. Besides, successive jumps and drops observed on the wear profile are always in the same order of magnitude as the tablet's thickness, suggesting some tablet's movements within the contact: hence, pieces of tablets are directly involved by the wear mechanism, as suggested by the SEM observations (Fig. 17d). However, the tablet pieces that are initially detached, are finally crushed within the contact which produces the non-cohesive tribolayer (Fig. 17b and e); this process maintains itself continuously. Hence, the crushing of the tablets – leading to nanodebris – seems to occur after the tablets' debonding. So, the *interlamellar* matrix is broken before the *intracrystalline* one, this would explain the high level of friction which is observed here.

To better understand this process, the previous FEM model is used again, but the initial impactor velocity is still reduced by a factor 10 in Fig. 18a, and finally set to zero in Fig. 18b in order to remove the shocks occurrence. For the sake of comparison with the above simulation (Fig. 12), the *interlamellar* matrix is again considered without any pores. As shown in the Fig. 18, the damage mechanism changes and the location of fracture progressively moves from the tablet to the *interlamellar* matrix when the impactor velocity is reduced. As a result, this latter is completely fractured, while the tablet remains intact after deformation and becomes free. In absence of shock – *i.e.*, in a quasi-static compression or shearing test (Fig. 18b) – high shear region and crack propagation may only be located inside of the *interlamellar* organic matrix. Besides, time-history evolution of the stress reveals that this mechanism needs more energy than that of the nanoshocks (Fig. 13) because it involves the *interlamellar* matrix, which is 4 times stiffer than the *intracrystalline* one

(see Table 1). Nanoshocks mechanism (Fig. 18a) involves stress peaks which are very sharp whereas *interlamellar* damage mechanism rather involves a continuous peeling of the matrix (Fig. 18b). Once in the contact, the detached tablets are completely crushed into homogeneous wear debris, as reported on various SEM views (Fig 17e). As a result, the amount of the wear debris trapped within the contact is also very important – and so the wear rate. In presence of porosity, the average size of debris is of course much more dispersed as shown above.

Consequently, the main wear mechanism in the nanotribological *high frictional regime* involves the fracturing of both organic matrices as a continuous mechanism. The high frictional energy is mainly dissipated by fracturing the *interlamellar* matrix, explaining the high level friction coefficient recorded during the test. The continuous tribolayer – which is initially constituted by huge debris and pieces of fractured tablets – is progressively built up by crushing the fractured tablets into homogeneous nanodebris. So, this mechanism also involves the damage of the *intracrystalline* matrix, but as a secondary process.

### 3.2.2 Nanotribological tests involving the low frictional regime (down to $\mu\text{W}$ )

Typical *in situ* tribological behavior is reported in Fig 19 (the average dissipated power is around  $5.5 \mu\text{W}$ ). In contrast to what is observed in the previous *high frictional regime*, *power map* (Fig. 19a) is here very smooth along the friction track and with time. The dissipated power is reduced by a factor 4 with respect to the *high frictional regime* (around  $21\mu\text{W}$ ). This difference is very close to the ratio between the strengths of the organic matrices (see Table 1 and [14]). Thus, a change of wear mechanism – that would involve the fracturing of *intracrystalline* instead of *interlamellar* matrix – is surely expected. Wear map (Fig. 19b) is also quite homogeneous but reveals that a cohesive tribolayer is now continuously built-up during the test. It is never removed during the tests, in contrast to what is observed for the *high frictional regime*. The cohesion ability of tribolayers being generally linked to the size of the elemental wear debris that constitute them, AFM image analysis reveals that their size is very close to the one of the initial nanograins constituting the biocrystals (Fig. 19e vs. Fig.1e). Wear profile extracted from *wear map* (Fig. 19c) also confirms the presence of a very thin tribolayer whose thickness is seldom over the initial tablet's thickness (above 500 nm). That

means here that only one layer of tablets is involved in the wear process. This result is also suggested in typical SEM pictures (Fig. 19d). Thus, in that case, the wear mechanism would be mainly a fracturing within the tablet, involving the *intracrystalline* organic matrix only (mainly composed by silk-fibroin-like proteins). That would explain the connection between the reduction of the frictional dissipated power and the difference between the matrices' stiffness, as mentioned above. Thus, the main wear mechanism clearly involves the detachment of nanograins of the biocrystals from the top row of tablets by breaking of the *intracrystalline* organic matrix. Wear debris – close to the nanograins (Fig. 19e) – are directly generated, without any debonding the tablets as previously observed in the *high frictional regime*. Hence, tablets' debonding mechanism could be likely the driving force controlling the transition from the low to the high regime (Fig. 15b). Let us check this assumption out.

### 3.2.3 Transition from low to high frictional regime as the gap between nano- and macro-scale

As reported in Fig. 15b, the transition between the *low frictional regime* and the *high frictional* one is quite irreversible and, is only observed in the *face-on* configuration – *ie* when the tablets are oriented more or less parallel to the direction of sliding (see Fig. 18b). In contrast, when tablets are no longer flat but upright on the section, and parallel to the direction of sliding – so-called *edge-on* configuration – the *low frictional regime* is always observed in a large range of dissipated powers [29]. So, this transition only seems to be controlled by the shear resistance of the *interlamellar* matrix. Referring to recent results carried out on *face-on* configuration of sheet nacre [29], friction and wear are very sensitive to the track smoothness. As long as the crack is still below a critical size (close to the tablets' thickness), fracturing mainly occurs within the tablets involving the *intracrystalline* matrix only (Fig. 19c). But as soon as the crack's thickness overshoots the critical size (Fig. 17c), the fracturing location moves from the *intracrystalline* matrix to the *interlamellar* one. As a result, the frictional dissipation power suddenly increases because the two matrices are now involved, but the influence of the *intracrystalline* is almost imperceptible, completely hidden by the *interlamellar* one.

So, the *high frictional* regime clearly makes the connection between the low and high dissipated power process that is, between the nanotribological and the macrotribological tests: as same coefficients of friction, and wear rate which depends on the friction dissipated power. The transition is only observed as soon as the *interlamellar* matrix is broken. Thus, this frictional power-induced transition is clearly the key connecting tribological process from nano- to macroscale, which is controlled by the shear resistance of the “*interlamellar*” matrix (polysaccharides in between the tablets).

#### 3.2.4 Tribological tests involving the ultralow frictional regime (down to nW)

As shown in Fig. 20a, the friction coefficient drops when the frictional dissipated power decreases until several nW – by decreasing the sliding velocity. Wear rate is too low to control the dissipated frictional power, as mentioned above. So, any variation of the sliding velocity involves a change of the friction coefficient. However, an anisotropic effect is clearly observed when the orientation of the sample is switched from *face-on* to *edge-on* configuration. In the *face-on* configuration, stick-slip phenomenon – due to the elastic recovery of the structure – is clearly observed at very low sliding speeds (Fig. 20b), locking the friction coefficient drop around 0.09 whatever the frictional dissipated power down to the nW. The blue curve (in Fig. 20b) also reveals a low dissipative wear mechanism that is clearly coupled with the stick-slip phenomenon and probably controlled by the elastic properties of the organomineral tablets – *ie.* the *intracrystalline* matrix itself.

In contrast, same tribological tests, which are carried out in the *edge-on* configuration, reveal that the friction coefficient continuously drops when the sliding velocity decreases. In addition, no stick-slip phenomenon is observed in that configuration. Thus, for the same sliding speed, the friction coefficient is much lower in the *edge-on* configuration than in the *face-on* one because elastic dissipation and wear process are here replaced by an *irreversible* deformation that could be connected to the plasticity of the organomineral tablets (Fig. 20c). Hence, the dissipative frictional power is much lower, and so the wear rate. The reduction of the friction coefficient is probably due to the transfer of the organic component – as a lubricant and protective film – on the friction interface, as suggested by Jia *et al* [31] using EDX analysis of the friction track.

Since the *edge-on* configuration seems to be the best one for any sheet nacre tribological applications, friction tests have been finally carried out at 70  $\mu$ W on over 5000 cycles in order to check the lifespan (Fig. 21). As expected, the initial contact involves a vertical displacement of about 80 nm under the slider. This deformation could result of some plastic deformations within the vertical organomineral tablets as mentioned above for the short tribological tests – ie., 100 cycles. However, Fig.21 suggests that this initial “plastic” displacement is not at all permanent since the wear profile increases over the first thousands cycles until the complete surface recovery. This means that the contact is rather submitted to very long recovery-time viscoelastic deformations within the tablets [16, 48] – ie., several hundreds cycles. As a result of the viscoelastic contact deformation the friction coefficient strongly oscillates during this period. But, as soon as the wear profile reaches its initial value – ie.,  $z = 0$  nm – the friction coefficient decreases abruptly on over 1000 cycles because of an increasing tribolayer-induced lubricant that is progressively built within the contact [31]. Finally, the coefficient of friction stays low and stable until the end once the film’s thickness reaches an uniform value – which is about 60 nm. Thus, the *edge-on parallel* configuration seems clearly the best way to succeed in the nacre-like bioprosthetic design displaying a high lifespan.

#### 4. CONCLUSION

*Multiscale* tribological behavior of *face-on* sheet nacre has been studied by varying the frictional power which is dissipated within the contact. Results reveal various dissipative mechanisms controlled by the two organic matrices on various scales:

- When the frictional dissipated power is higher than 17 mW, wear of sheet nacre is mainly controlled by thermal effects – combining melting of the organic matrices and friction-induced phase transformation of the mineral phase. These two mechanisms start from 17 mW and 49 mW, respectively. Beyond, the wear rate dramatically increases as a so-called *avalanche effect* due to the propagation of the heat flow within the subsurfaces, damaging matrices in depth.



- When the frictional dissipated power is in between 1  $\mu$ W and 17 mW, wear is mainly controlled by a friction-induced nanoshock process involving the fracture of the *intracrystalline* matrix only. However, this process can be preceded (or not) by the fracture of the *interlamellar* one increasing (or not) the frictional dissipated power by a factor 4 or more. The *interlamellar* damage occurrence clearly controls the transition from low to high frictional regime and then, the wear rate on a large range. This irreversible transition is completely controlled by the shear resistance of the *interlamellar* matrix, and obviously depends on the orientation of the sheet nacre (*face-on* vs. *edge-on* configuration)
- When the friction dissipated power is decreased down to 1 nW, the tribological behavior is completely controlled by the orientation of the samples (*face-on* vs. *edge-on*), and so by the organic matrices. In *face-on* configuration, stick-slip occurrence simultaneously controls friction and wear behaviors. In contrast, in *edge-on* configuration, an interesting lubricant effect – probably due to an organic tribolayer generated by the organic *interlamellar* phase – is observed in association with some viscoelastic deformations of the organomineral tablets. This orientation leads to the better tribological behaviour displaying a low and stable friction coefficient along thousands cycles without any detectable wear ;

## ACKNOWLEDGEMENTS

This work was supported by grants from the Agence Nationale de la Recherche Française under the awards NanoBioCarbonate ANR 10 INTB 90901 *Organic mediation on nanostructured biomaterials, biomimetic example of otoliths and freshwater pearls*. Authors are grateful to Mr. Philippe Violle from Sympatec GmbH for lending the PCCS Nanophox equipment which allowed us the multiscale wear debris assessment.

## REFERENCES

- [1] M. Lee, *Mother-of-Pearl: An Engineering Gem in Remarkable Natural Material Surfaces and Their Engineering Potential*, M. Lee (Ed), (2014) Springer International Publishing, ISBN 978-3-319-03124-8
- [2] M. A. Meyers, P-Y. Chen, A. Yu-Min Lin, Y. Seki, *Biological materials, Structure and mechanical properties*, Progress in Materials Science 53 (2008) 1-208
- [3] Y. Levi-Kalisman, G. Falini, L. Addadi, S. Weiner, *Structure of the nacreous organic matrix of a bivalve mollusc shell examined in the hydrated state using cryo-TEM*, J. Structural Biology, 135, (2001), 8-17 ;
- [4] X.Li, W-C. Chang, Y. J. Chao, R. Wang, M. Chang, *Nanoscale structure and mechanical characterization of a natural nanocomposite material : the shell of red abalone*, Nanoletters, 4, 2004, 613-617
- [5] M. Rousseau, E. Lopez, Ph. Stempflé, M. Brendlé, L. Franke, A. Guette, R. Naslain, X. Bourrat, *Multiscale structure of sheet nacre*, Biomaterials, 26, 2005, 6254-6262
- [6] X. Li, Z. Huang, *Unveiling the formation Mechanism of Pseudo-Single-Crystal Aragonite Platelets in Nacre*, Physical Review Letters, 102, 075502, (2009)
- [7] H.D Espinosa, J.E. Rim, F. Barthelat, M.J. Buehler (2009), *Merger of structure and material in nacre and bone – persepectives on de novo biomimetic materials*, Prog Mater sci 54 (8): 1059-1100
- [8] B. Denkena, J. Koehler, A. Moral (2010) *Ductile and brittle material removal mechanisms in natural nacre – a model for novel implant materials*, J. Mater. Proc Technol 210 (14): 1827-1837
- [9] A. Dutta, S. A. Tekalur, M. Miklavcic, *Optimal overlap length in staggered architecture composites under dynamic loading conditions*, Journal of the Mechanics and Physics of Solids 61 (2013) 145-160;
- [10] J. Vincent, *Structural Biomaterials*, Princeton University Press, (1990), ISBN 978-0691025131
- [11] D.L. Kaplan (1998), *Mollusc shell structures: novel design strategies for synthetic materials*, Curr. Opin Solid State Mater Sci 3 (3):232-236
- [12] R.Z. Wang, Z. Suo, A.G. Evans, N.Yao, I.A. Aksay, (2001) *Deformation mechanisms in nacre*, J. Mater Res 16 (9): 2485-2493

- [13] A. Dutta, S. A. Tekalur, *Crack tortuosity in nacreous layer – Topological dependence and biomimetic design guideline*, International Journal of Solids and Structures 51 (2014) 325-335;
- [14] Ph. Stempflé, O. Pantalé, M. Rousseau, E. Lopez, X. Bourrat, *Mechanical properties of the elemental nanocomponents of nacre structure*, Materials Science and Engineering C 30 (2010) 715–721
- [15] L. Peireira-Mouriès, M.J. Almeida, C. Ribeiro, J. Peduzzi, M. Barthélémy, C. Milet, E. Lopez. *Soluble silk-like organic matrix in the nacreous layer of the bivalve Pinctada maxima—a new insight in the biomineralization field*. Eur J Biochem 2002;269:4994–5003.
- [16] Z-H Xu, X. Li, *Deformation strengthening of biopolymer in nacre*, Adv. Funct. Mater., 2011, 21, 3883-3888
- [17] E. Munch, M.E. Launey, D.H. Alsem, E. Saiz, A.P. Tomsia, R.O. Ritchie, Tough bio-inspired hybrid materials, Science 322 (2008) 516-520
- [18] GM. Luz, J.F. Mano (2009), Biomimetic design of materials and biomaterials inspired by the structure of nacre, Philos Trans Math Phys Eng Sci 367 (1893): 1587-1605
- [19] D. Zhu, F. Barthelat, (2011) *A novel biomimetic material duplicating the structure and mechanics of natural nacre*, in Proulx T (ed) Mechanics of biological systems and materials, vol 2. Springer, NY
- [20] Z. Tang, N.A. Kotov, S. Magonov, B. Ozturk, (2003) Nanostructured artificial nacre, Nat Mater 2: 413-418
- [21] G. Atlan, O. Delattre, S. Berland, A. Lefaou, G. Nabias, D. Cot, E. Lopez (1999) *Interface between bone and nacre implants in sheep*, Biomaterials 20 (11): 1017-1022
- [22] E. Lopez, S. Berland, C. Camprasse, G. Camprasse, C. Silve, *Demonstration of the capacity of nacre to induce bone formation by human osteoblasts maintained in vitro*. Tissue Cell 1992;24:667–79.
- [23] P. Westbroek, F. Marin, *A marriage of bone and nacre*, Nature 392, 1998,861-862
- [24] A. Yu-Min Lin, M. A. Meyers, *Interfacial shear strength in abalone nacre*, J. of the mechanical behavior of biomedical materials 2, (2009) 607-612
- [25] Ph. Stempflé, M. Brendlé, *Tribological behaviour of nacre – Influence of the environment on the elementary wear processes*, Tribology International 39, 2006, 1485-1496

- [26] Ph. Stempflé et al, *Friction-induced sheet nacre fracture : effects of nanoshocks on cracks location*, Int. J. Nanotechnol., Vol. 4, N°6, 2007, 712-729
- [27] Ph. Stempflé, T. Djilali, R. Kouitat Njiwa, M. Rousseau, E. Lopez, X. Bourrat *Thermal-induced wear mechanisms of sheet nacre in dry friction*, Tribology Letters, 2009, 35 : 97-104 ;
- [28] Ph. Stempflé, O. Pantalé, T. Djilali, Richard Kouitat Njiwa, X. Bourrat, J. Takadoum, *Evaluation of the real contact area in three-body dry friction by micro-thermal analysis*, Tribology International, 43, 2010, 1794-1805
- [29] Ph. Stempflé, X. Bourrat, M. Rousseau, E. Lopez, J. Takadoum, *Nanotribology of nacre: Anisotropic dissipation in a multiscale hybrid material*, Tribology International 63 (2013) 250–264
- [30] X. Tian, Z. Han, X. Li, Z. Pu, L. Ren, *Biological coupling anti-wear properties of three typical molluscan shells – Scapharca subcrenata, Rapana venosa, Acanthochiton rubrolineatus*, Science China, 2010, Vol. 53, N°11:2905-2913
- [31] X. Jia, X. Ling, D. Tang, *Microstructure and friction-wear characteristics of bivalve shells*, Tribology International, 39, 2006, 657-662
- [32] X. Bourrat, L. Francke, E. Lopez, M. Rousseau, Ph. Stempflé, M. Angellier, P. Albéric, *Nacre biocrystal thermal behavior*, CrystalEngComm 9, 2007, 1205-1208
- [33] Z. Huang, X. Li, *Nanoscale structural and mechanical characterization of heat treated nacre*, Materials Science and Engineering C 29 (2009) 1803-1807
- [34] A. Briggs, O. Kolosov, *Acoustic Microscopy*, 2<sup>nd</sup> Ed, (2009), OXFORD University, ISBN: 9780199232734
- [35] R. Gr. Maev, *Acoustic Microscopy: Fundamentals and Applications*, Wiley-VCH, ISBN: 978-3-527-40744-6
- [36] L. Robert, N. Brunet, T. Flaherty, T. Randles, E. Matthaei-Schulz, H. Vettters, D. Rats, J. von Stebut, *Characterisation of TiN and carbon-doped chromium thin film coatings by acoustic microscopy*, Surface and Coatings Technology 116–119 (1999) 327–334

- [37] C. Comte, J. von Stebut, *Microprobe-type measurement of Young's modulus and Poisson coefficient by means of depth sensing indentation and acoustic microscopy*, Surface and Coatings Technology 154 (2002) 42–48
- [38] Z-H. Xu, Y. Yang, Z. Huang, X. Li, Elastic modulus of biopolymer matrix in nacre measured using coupled atomic force microscopy bending and inverse finite element technique, Materials Science and Engineering C31 (2011) 1852-1856
- [39] Z.M. Zhang, *Nano/Microscale Heat Transfer*, McGraw Hill, (2007), ISBN 978-0-07-143674-8
- [40] C-Y Wang, S-P Pan, G-S Peng, J-H Tsai, *A comparison study on the measurement of nanoparticles*, Proc. SPIE 5879, *Recent Developments in Traceable Dimensional Measurements III*, 587910 (19 August 2005); doi: 10.1117/12.616440
- [41] L. Theodore, *Nanotechnology – Basic Calculations for engineers and scientists*, (2006), Wiley, ISBN-13: 978-0-471-73951-7
- [42] Ph. Stempflé, J. Takadom, *Multi-asperity nanotribological behaviour of single-crystal silicon: Crystallography-induced anisotropy in friction and wear*, Tribology International 48, 2012, 35-43
- [43] Ph. Stempflé, R. Kouitat Njiwa, *In situ running-in wear assessment in multi-asperity nanotribology*, Wear 328-329 (2015) 77–88
- [44] ABAQUS – *ABAQUS Standard User Manual*, V. 6.8, in Hibbitt, Karlsson, Sorensen (HKS) Inc (editors), 1997, Rhode Island, USA
- [45] B. Ji, H. Gao, *Mechanical properties of nanostructure of biological materials*, J. Mech. Phys. Solids, Vol. 52, (2004), 1963–1990.
- [46] Ph. Stempflé, J. von Stebut, *Nanomechanical behaviour of the 3<sup>rd</sup> body generated in dry friction – Feedback effect of the 3<sup>rd</sup> body and influence of the surrounding environment on the tribology of graphite*, Wear 260, 2006, 601-614
- [47] M. Rousseau, A. Meibom, M. Gèze, X. Bourrat, M. Angellier, E. Lopez, (2009) *Dynamics of Sheet Nacre Formation in Bivalves*, Journal of structural biology, Vol. 165, pp 190-195
- [48] M.A. Meyers, A. Yu-Min Lin, P-Y Chen, J. Muiyco, *Mechanical strength of abalone nacre: Role of the soft organic layer*, J. of the mechanical behavior of biomedical materials I (2008), 76-85

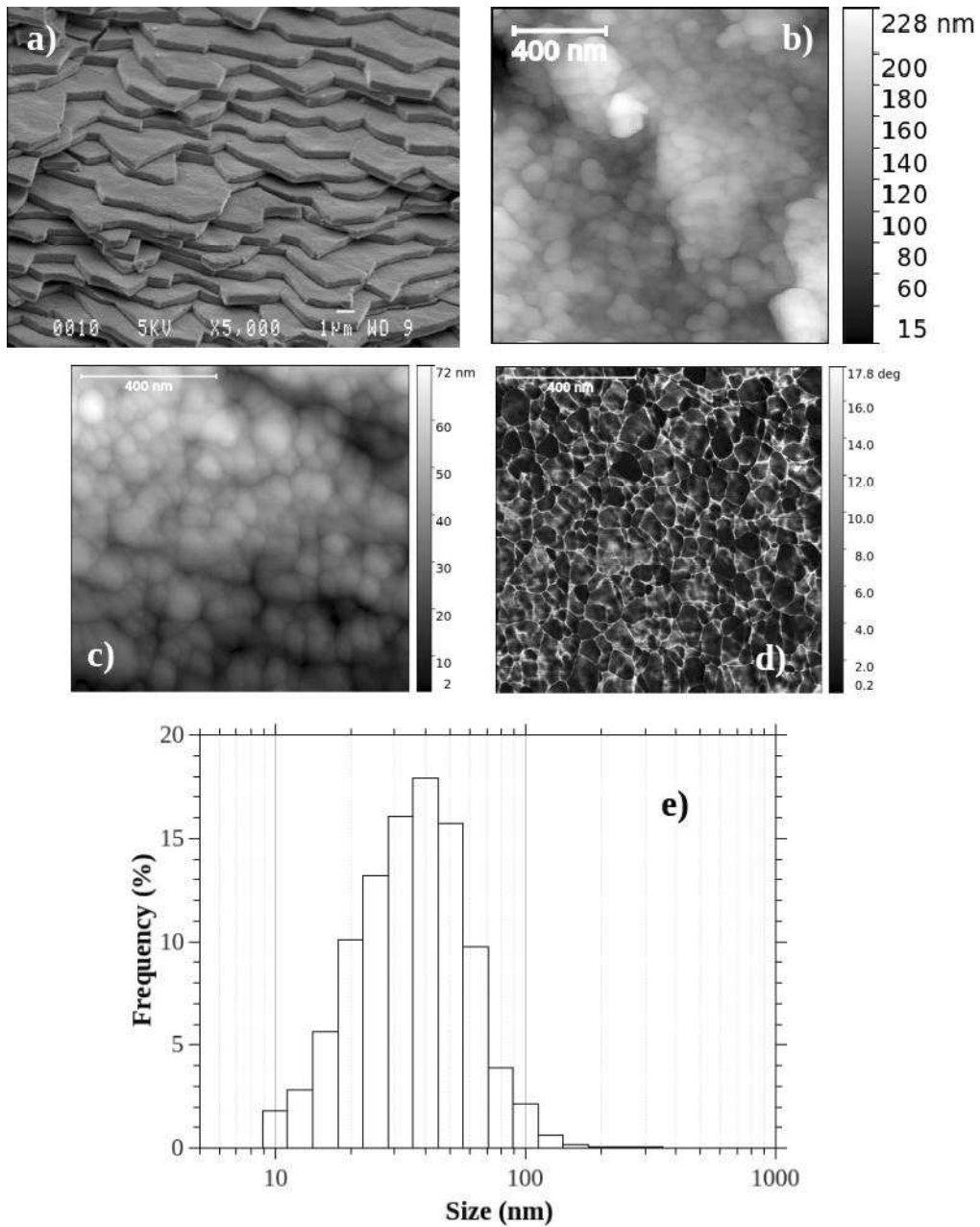


Figure 1 : Multiscale structure of nacre a) the brick & mortar architecture ; b) enlargement on the edge of a brick revealing biocrystals ; Typical AFM views of the polished top surface of an aragonite platelet observed in tapping-mode: (c) Height map ; and (d) phase contrast map. These maps reveal the nanosized biocrystals of  $\text{CaCO}_3$  surrounded by the intracrystalline organic matrix ; e) distribution in size of the biocrystals constituting tablets after image analysis on AFM maps

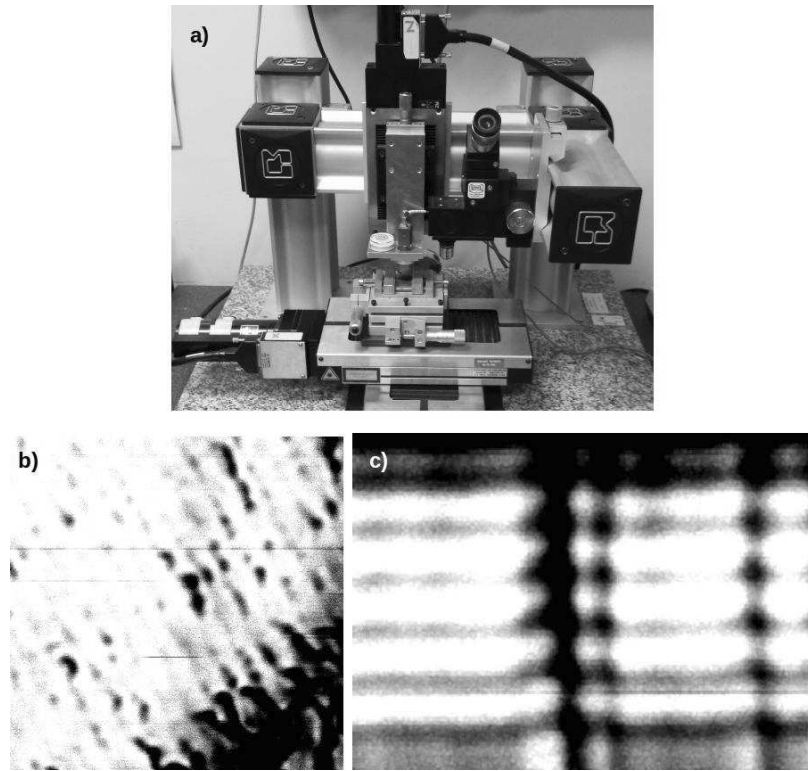


Figure 2 : a) Acoustic microscope ; b) Acoustic imaging of face-on sheet nacre sample (482 MHz, at  $z = 0$   $\mu\text{m}$ ) and c) Acoustic micrograph of its sub-surface revealing the stacked structure

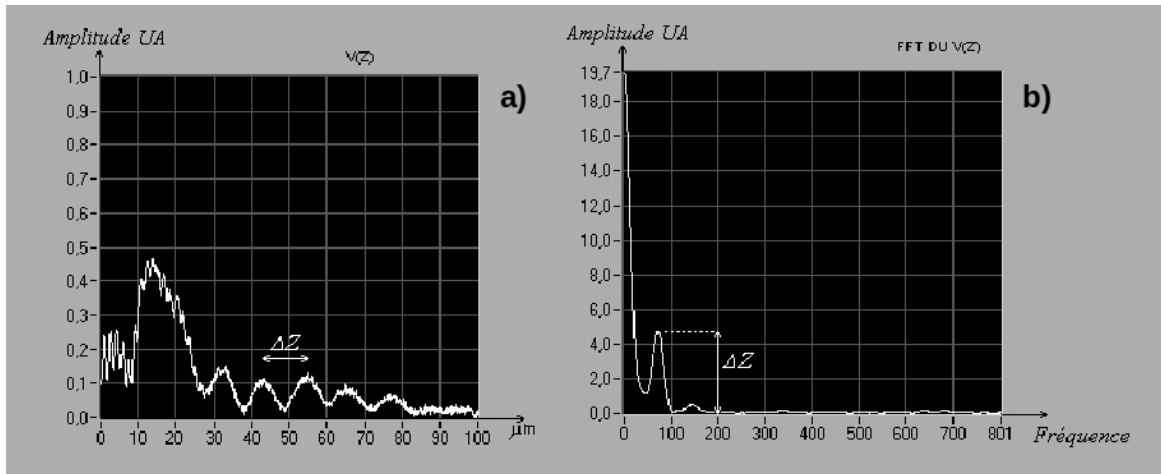
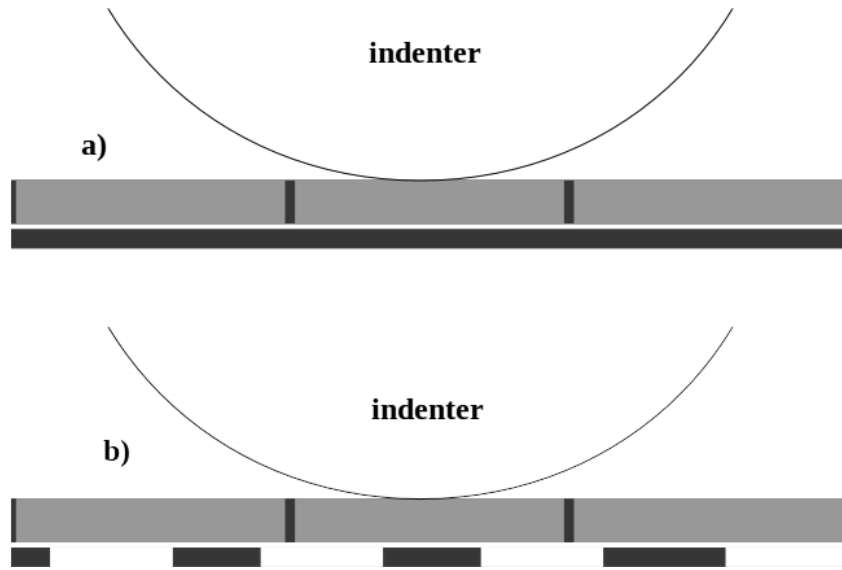


Figure 3 : Acoustic Signature Mode : a) pseudo periodicity  $V(z)$  curve connected to a specific surface acoustic wave velocity ; b) Fourier transform of  $V(z)$  from which the Rayleigh velocity and the attenuation are deduced





*Figure 4: Stratified models used for identifying the elastic properties of the interlamellar matrix (dark grey) vs. those of the tablets (light grey) by using spherical nanoindentation: a) for a continuous matrix without any porosity and b) for a porous matrix with white voids*

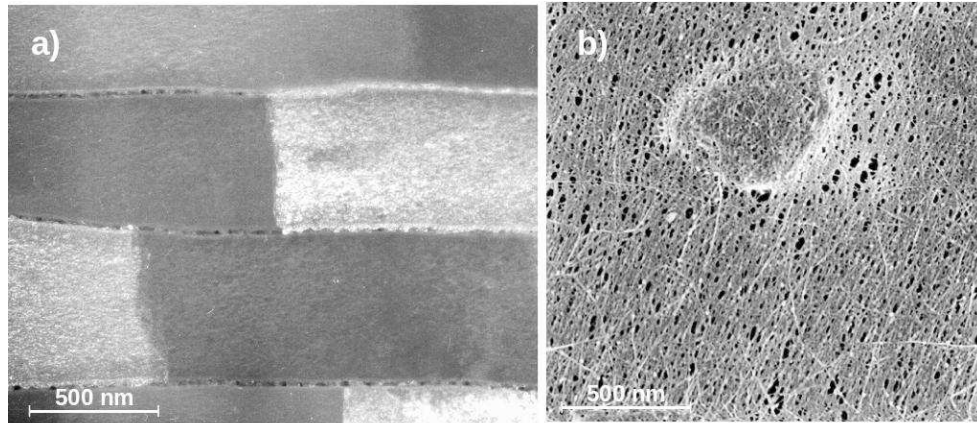


Figure 5: a) Darkfield TEM image of nacre. The organic matrix clearly appears porous. The real amount of interlamellar matrix is estimated as the bright continuous line along the tablets (6.47% of the tablet's volume). The crossed porosity appears in black as the darkfield (about 35% of the interlamellar area) ; b) SEM image of nacre growth front in *Pinctada margaritifera* showing the chitin-based interlamellar membrane with the nucleation of a tablet [47].

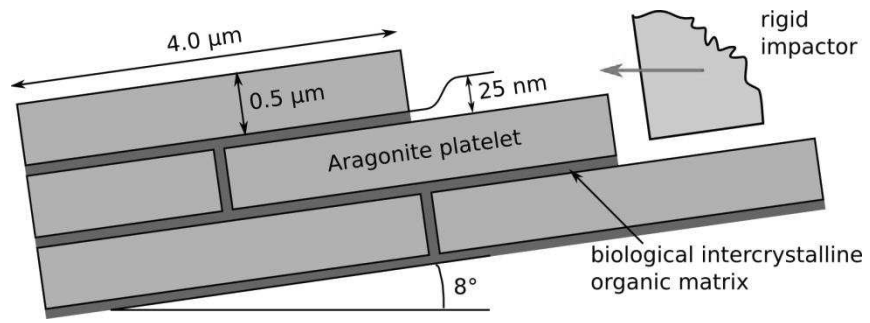


Figure 6: Finite element model simulating the wear mechanisms

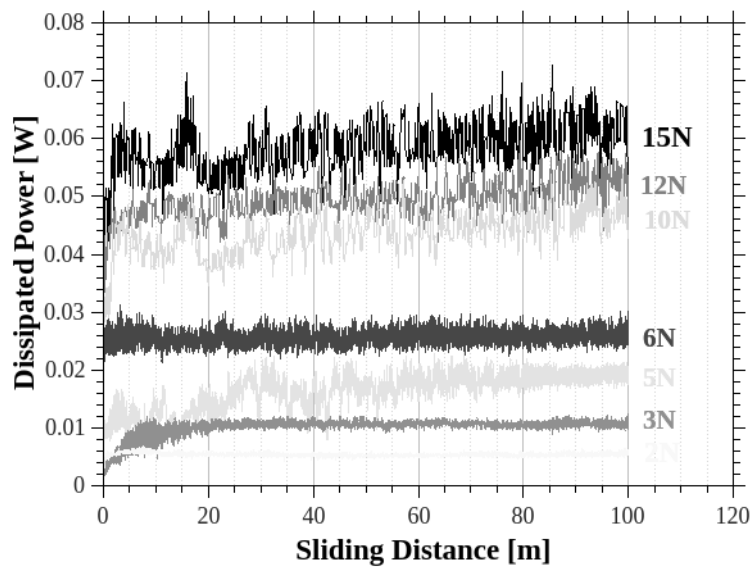


Figure 7: Variation of the dissipated power by friction vs. sliding length for various normal loads

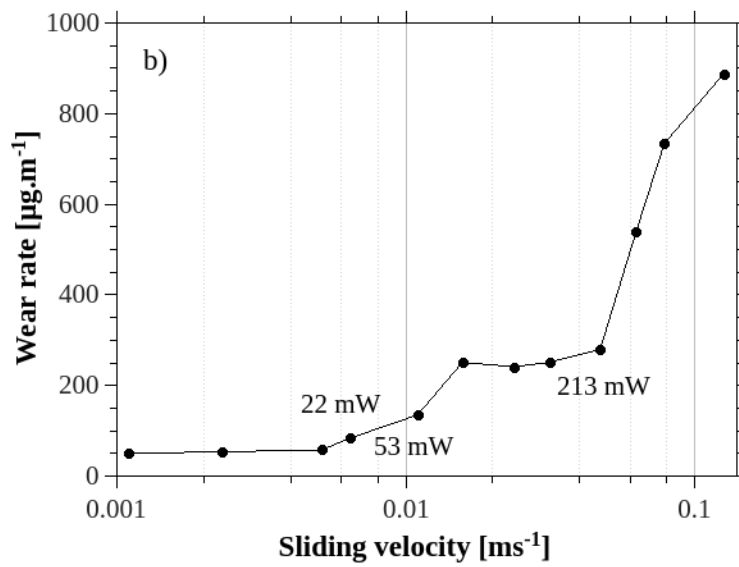
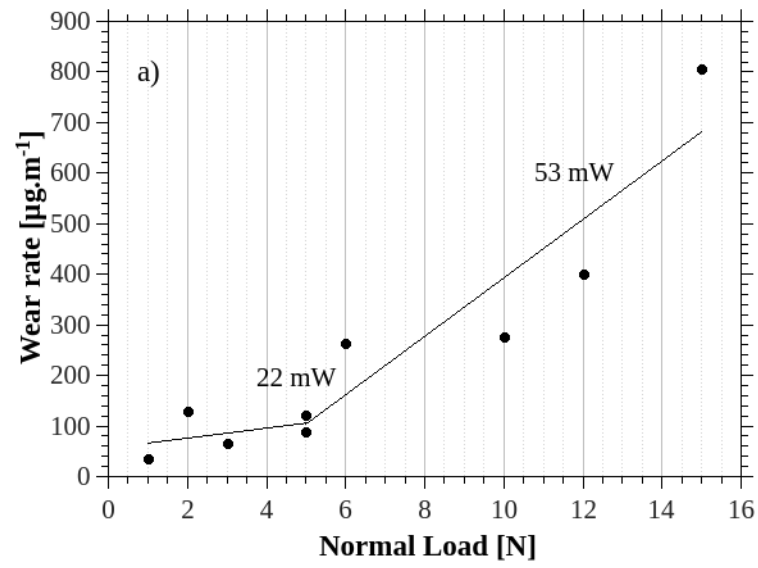


Figure 8: Variation of the wear rate with a) the normal load; b) the sliding velocity

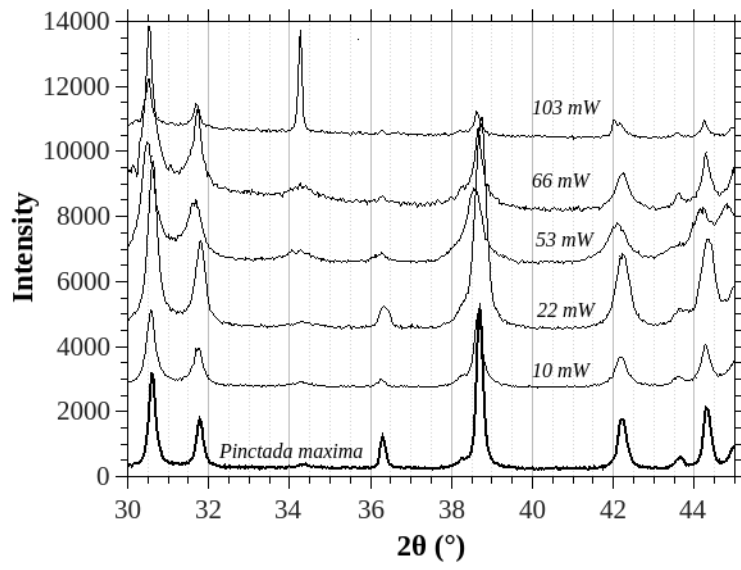


Figure 9: X-ray diffraction spectra of wear debris generated under various friction dissipated powers. The calcite peak is expected at  $34.28^\circ$

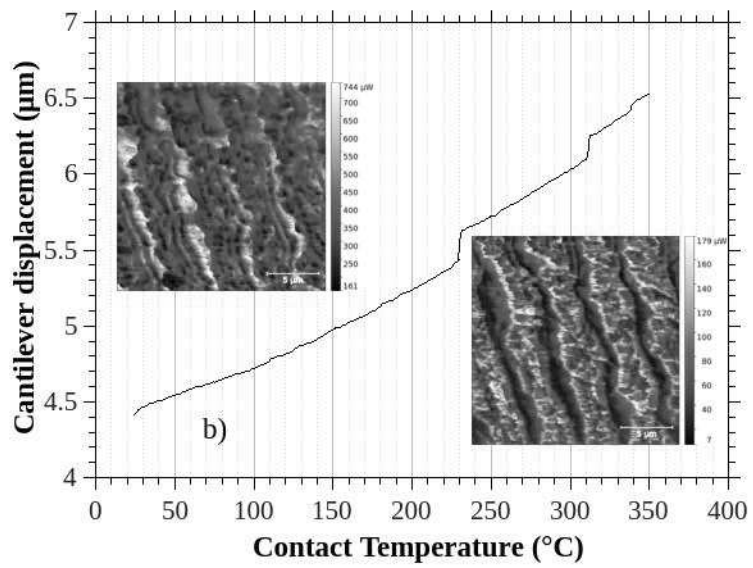
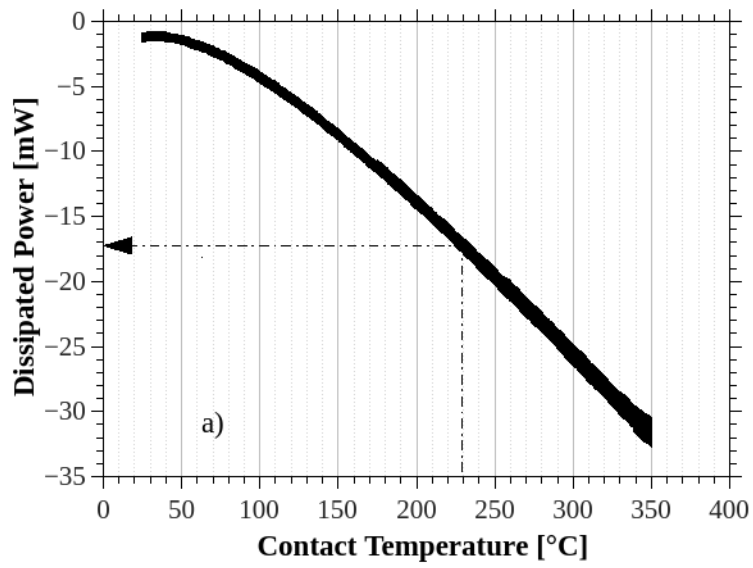


Figure 10: a)  $\mu$ DTA plot: dissipated power vs. contact temperature ( $T_c$ ) and; b)  $\mu$ TMA cantilever displacement vs. contact temperature; (inset) Typical AFM views of the same area observed before and after heating at 350°C

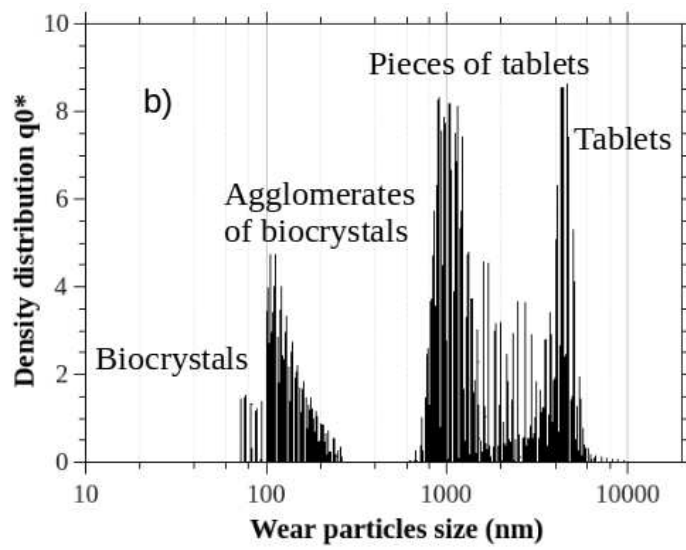
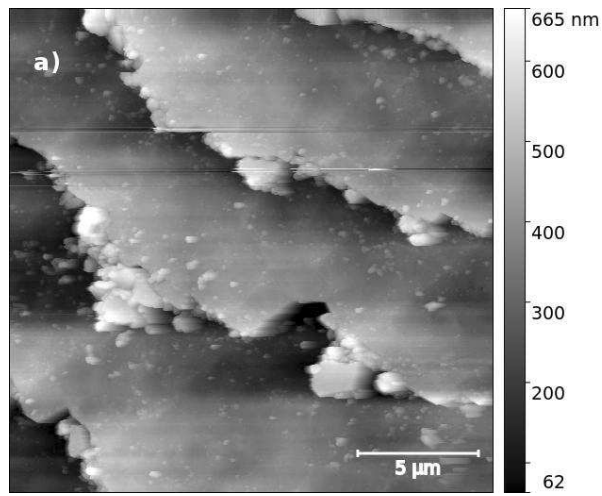


Figure 11: a) Typical AFM view of the friction track: the crumbling mechanism reveals the biocrystals constituting the tablets ; b) Particles size distribution of wear debris obtained by Photon Cross-correlation Spectroscopy



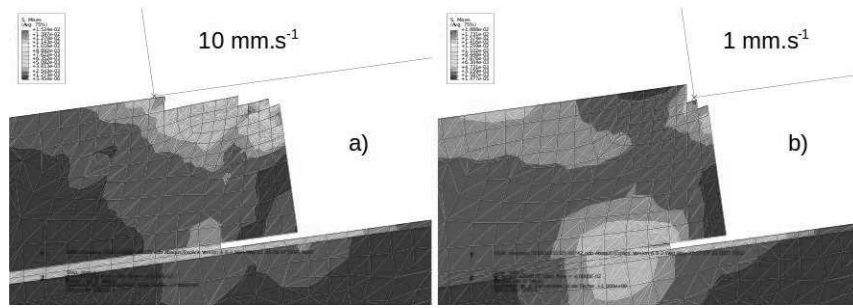
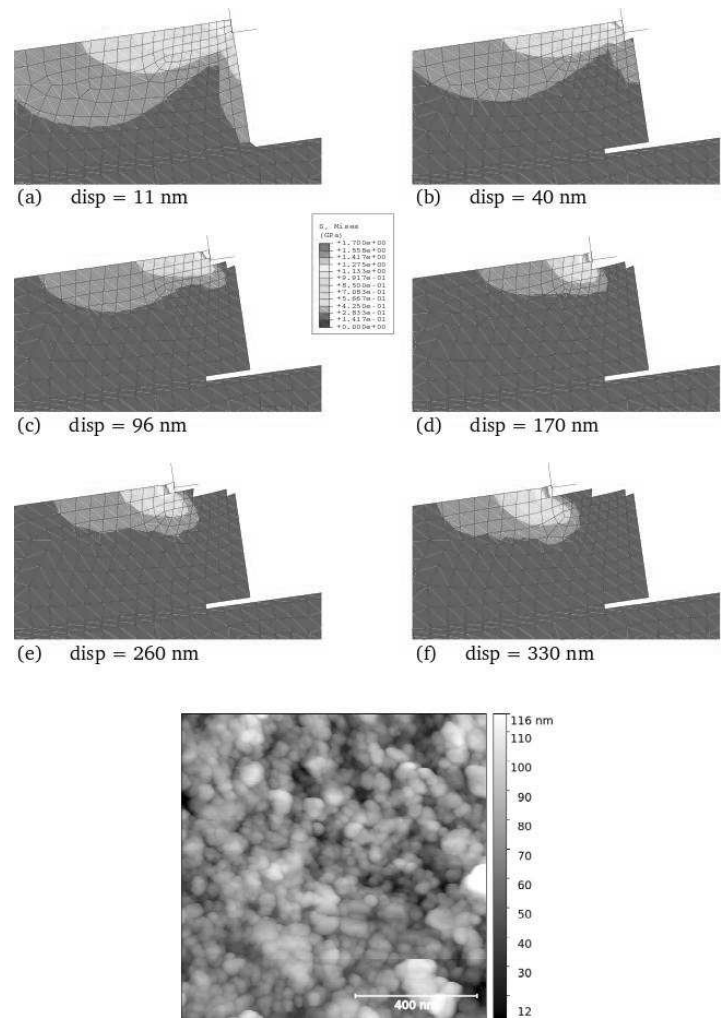
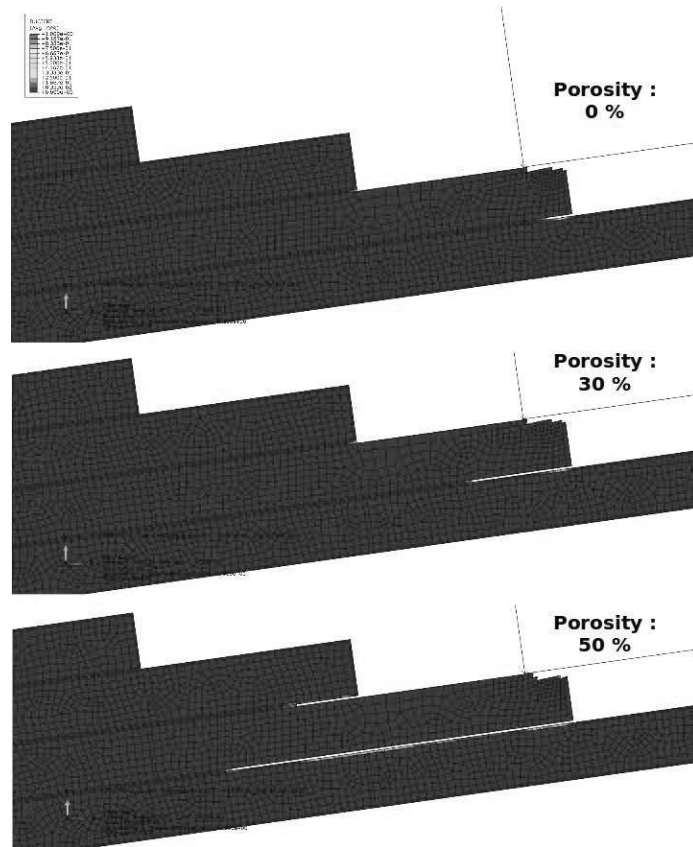


Figure 12: von Mises contourplot for two simulations (at  $4 \cdot 10^{-2}$  s) involving the nanoshocks effect: a) 10 mm/s and b) 1 mm/s on flat-on tablets of sheet nacre and c) formation of nanodebris



*Figure 13: Evolution of the von Mises contourplot for increasing penetration lengths (10 mm/s). These pictures well-illustrate the shock-induced wear mechanism which occurs in a large range of dissipated frictional power. This mechanism leads to the formation of nanodebris very close to the initial biocrystals constituting the tablets, as shown in the AFM view*



*Figure 14 : von Mises contourplot for three simulations (at 10 mm/s) carried out for increasing amount of porosity (0%, 30 and 50%, respectively). The fracture moves from inside of tablet to inside of the interlamellar matrix as matrix's porosity increases.*

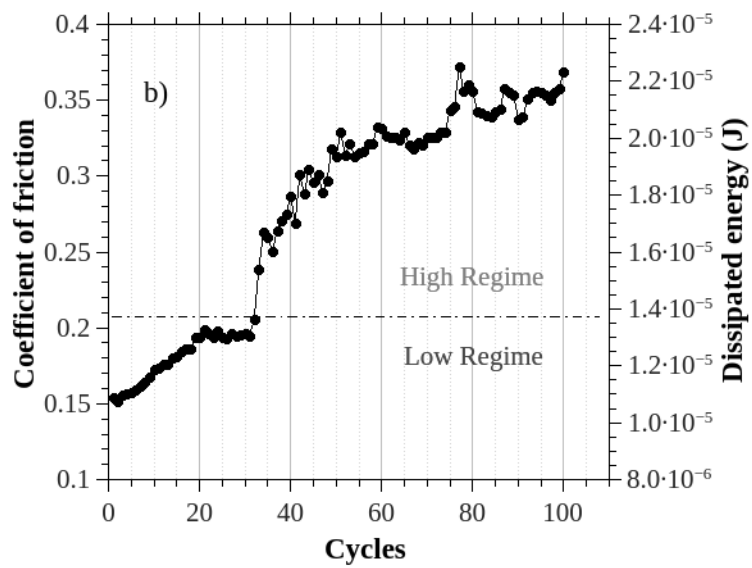
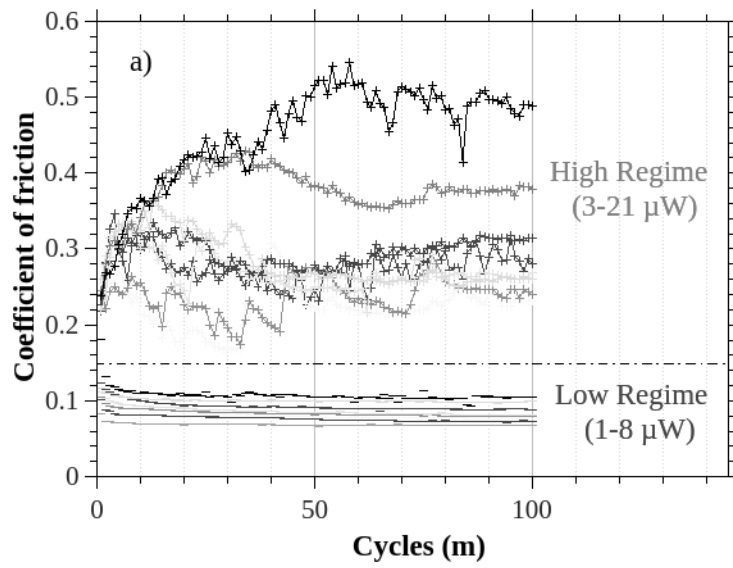
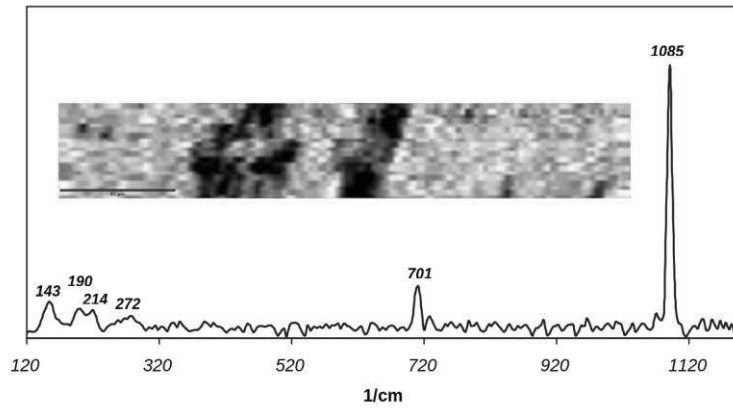


Figure 15: a) Evolution of the coefficient of friction with the normal load in high and low frictional regime, respectively; b) transition from low to high frictional regime due to the occurrence of a critical crack around 35 cycles (Normal load 30 mN)

Spectrum of aragonite



*Figure 16: Raman spectroscopy carried out on the friction track after a nanotribological test in high frictional regime. No thermal-induced phase transformation of aragonite to calcite is observed in contrast to what observed for macroscopic tribological tests*

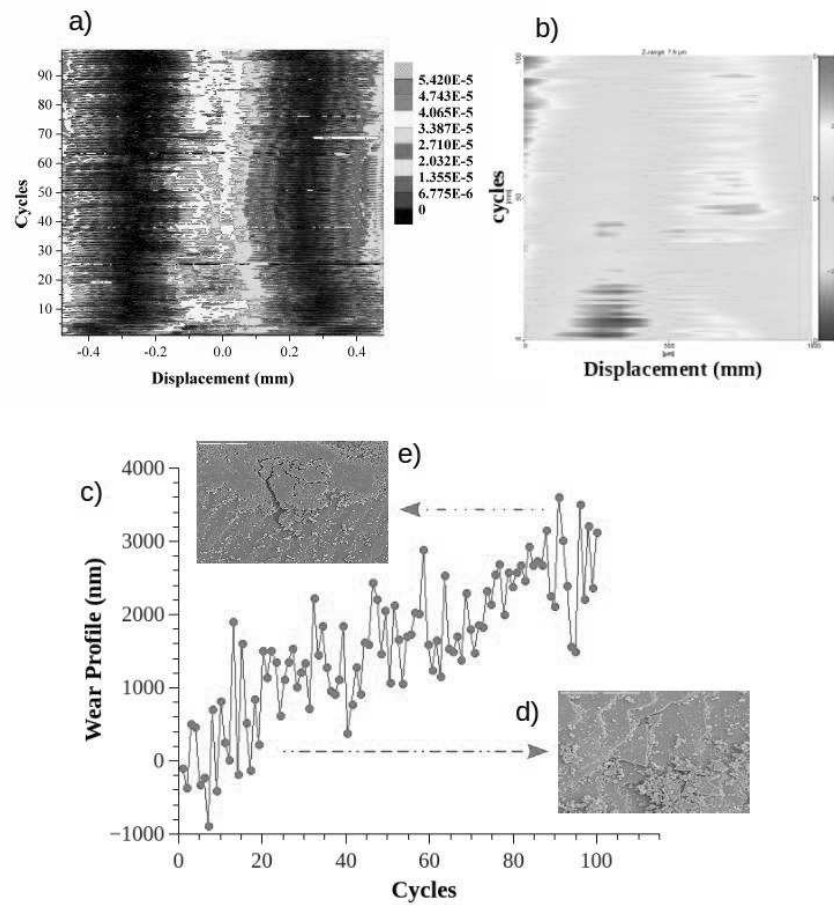


Figure 17: *in situ* tribological behaviour in high frictional regime at 70 mN: (a) Power map ; (b) Wear map ; (c) corresponding *in situ* wear profile assessment carried out in the center of the friction track; Morphology of the wear debris (d) at the beginning and, (e) at the end of the tribological test

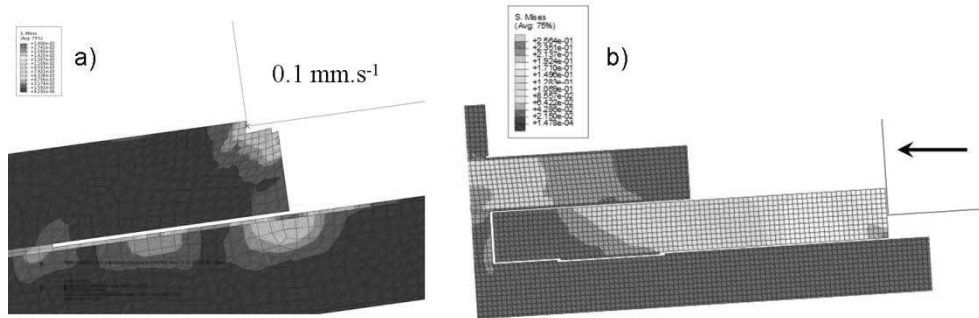


Figure 18: von Mises contourplot for two simulations: a) involving the fracture of both matrices at  $0.1 \text{ mm/s}$  and, b) involving the fracture of the interlamellar matrix only, when nanoshocks mechanism is avoided

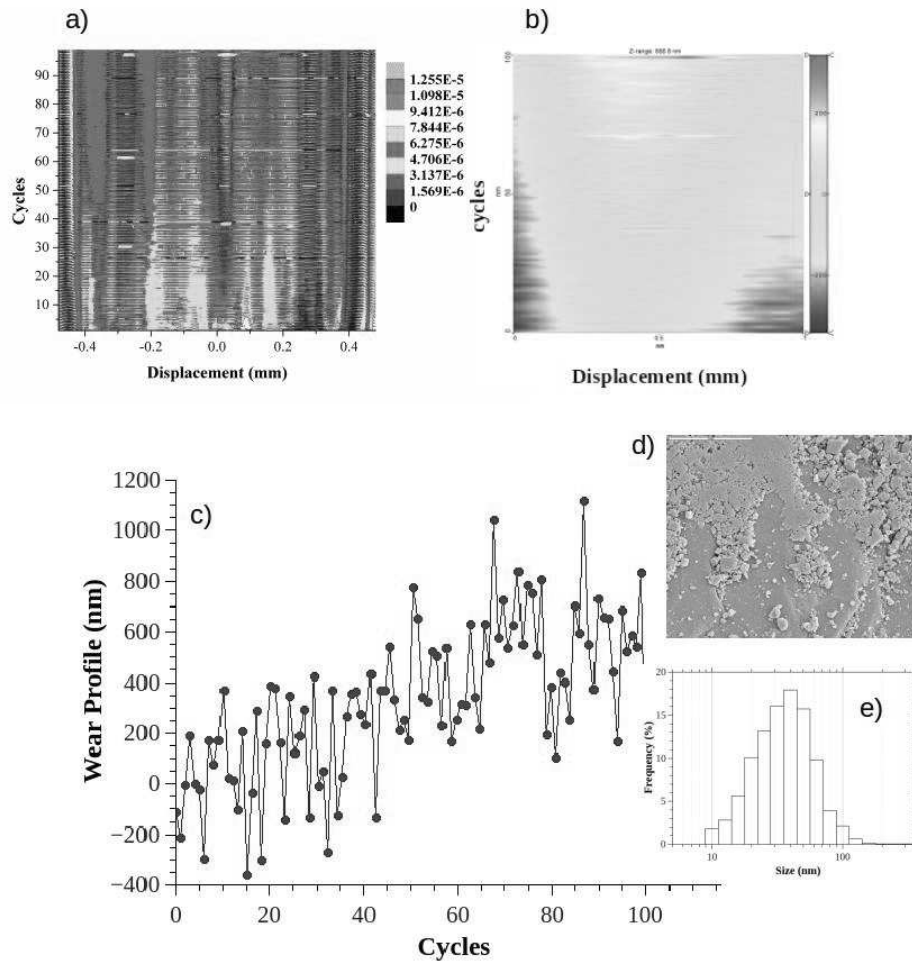


Figure 19: *in situ* tribological behaviour in low level regime at 70 mN: (a) Power map ; (b) Wear map ; (c) corresponding *in situ* wear profile assessment carried out in the center of the friction track; (d) Morphology of the wear debris at the end of the tribological test ; (e) distribution in size of the wear debris after image analysis on AFM maps



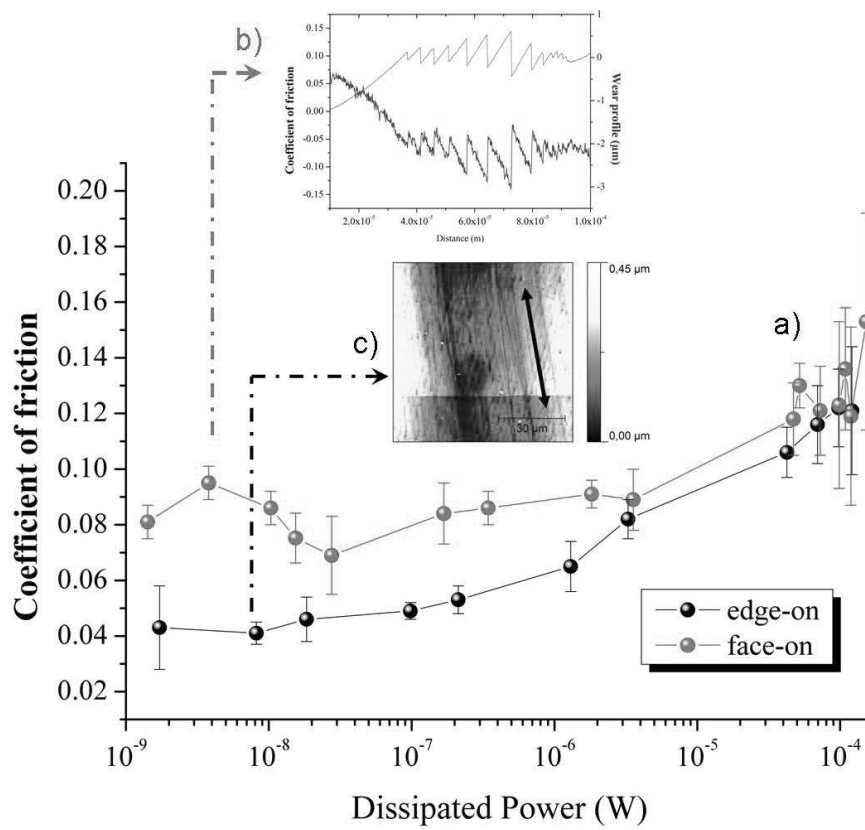
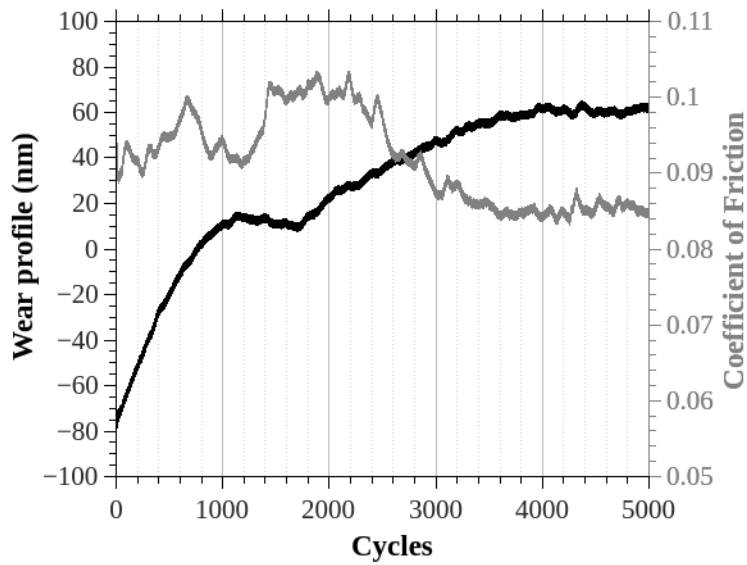


Figure 20 : a) Evolution of the coefficient of friction vs. dissipated power at ultralow nanotribological tests ;  
 b) evidence of a stick-slip phenomenon controlling the wear process (face-on configuration) ; c) Typical AFM view of the friction track after sliding revealing “irreversible” deformation of the tablets (edge-on configuration)



*Figure 21 : Lifespan test at 70  $\mu W$  in configuration edge-on parallel to the tablets orientation. It reveals that the initial “irreversible” displacement – as observed in Fig. 20c after only 100 cycles – is not permanent after thousands cycles. The contact is instead submitted to very long recovery-time viscoelastic deformations within the tablets. The coefficient of friction appears unstable until the complete surface recovering. As soon as the latter is done, an organic self-induced tribolayer lubricant locks the friction coefficient at a low and stable value without any wear [31].*

	E (GPa)	n	s <sub>y</sub> (GPa)	e <sub>max</sub> (%)
Organomineral tablets	58 ± 5% <sup>a)</sup>	0.2 (0.03) <sup>b)</sup> [14]	2.7 (0.7) <sup>b)</sup> [14]	1
	62.5 (11.2) <sup>b)</sup> [14]			
Biocrystals [14]	96.75 (5.67)	0.17 (0.05)	13.4 (2.1)	-
<i>interlamellar</i> matrix with 47% of porosity	6.308 (0.56) <sup>b)</sup> [26]	0.29 (1.2·10 <sup>-3</sup> ) <sup>b)</sup> [26]	0.119 (0.02) <sup>b)</sup> [26]	10 [45]
<i>interlamellar</i> matrix	13 ± 5% <sup>a)</sup>	0.29 (1.7·10 <sup>-3</sup> ) <sup>b)</sup> [26]	0.118 (0.02) <sup>b)</sup> [26]	10 [45]
	13.4 (0.79) <sup>b)</sup>			
<i>Intracrystalline</i> matrix [14]	3.81 (0.41)	0.296 (1.4·10 <sup>-3</sup> )	-	-
Brick & Mortar (nacre) [14]	54.42 (3.2) <sup>b)</sup>	0.25 (0.03) <sup>b)</sup>	-	-

<sup>a)</sup> from Acoustic Microscopy

<sup>b)</sup> from Spherical Nanoindentation

Table 1 : Mechanical properties of the *Pinctada maxima* sheet nacre and its components